THE JOURNAL OF PHYSICAL CHEMISTRY Letters

pubs.acs.org/JPCL Letter

Electronic Energy Relaxation in a Photoexcited Fully Fused Edge-Sharing Carbon Nanobelt

V. M. Freixas, N. Oldani, R. Franklin-Mergarejo, S. Tretiak, and S. Fernandez-Alberti*

Cite This: J. Phys. Chem. Lett. 2020, 11, 4711−4719 Read Online

ABSTRACT: Carbon nanobelts are cylindrical molecules composed of fully fused edge-sharing arene rings. Because of their aesthetically appealing structures, they acquire unusual optoelectronic properties that are potentially suitable for a range of applications in nanoelectronics and photonics. Nevertheless, the very limited success of their synthesis has led to their photophysical properties remaining largely unknown. Compared to that of carbon nanorings (arenes linked by single bonds), the strong structural rigidity of nanobelts prevents significant deformations away from the original high-symmetry conformation and, therefore, impacts their photophysical properties. Herein, we study the photoinduced dynamics of a successfully synthesized belt segment of (6,6)CNT (carbon nanotube). Modeling this process with nonadiabatic excited state molecular dynamics simulations uncovers the critical role played by the changes in excited state wave function localization on the different types of carbon atoms. This allows a detailed description of the excited state dynamics and spatial exciton evolution throughout the nanobelt scaffold. Our results provide detailed information about the excited state electronic properties and internal conversion rates that is potentially useful for designing nanobelts for nanoelectronic and photonic applications.

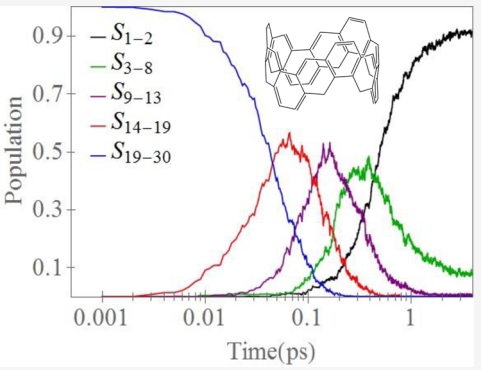

Carbon nanorings and nanobelts are cylindrical molecules originally synthesized to be used as templates for growing chirality-specific carbon nanotubes with desired optoelectronic properties, that is, with uniform diameters and sidewall structures (i.e., armchair, chiral, and zigzag structures).[1−8] Nevertheless, these structures are not limited to this particular application. In fact, such nanorings and nanobelts play central roles in supramolecular chemistry by forming molecular complexes with a variety of guests that fit the volume, shape, and environment of the cavity.[9−13] Moreover, the unusual molecular architectures of nanorings and nanobelts give rise to interesting physicochemical and electronic properties that can result in unpredictable applications in materials science and technology.[14] They constitute unusual nonplanar conjugated molecular systems in which the efficiency in π-orbital overlaps coexists with high strain energies and steric hindrances introduced by the cyclic nanostructure.[15−17] Altogether, these structural features confer nanorings and nanobelts with unusual optical absorption and emission properties.

Unlike carbon nanorings, composed of arenes linked by single bonds, the photophysics of fully fused edge-sharing carbon nanobelts remains relatively unexplored. This is due to the very limited success in their synthesis compared to the extensive studies focusing on the synthesis and characterization of cycloparaphenylenes (CPPs) and related carbon nanorings.[18−39] A few previous theoretical studies performed on different nanobelts and [n]cycloacenes[17,40,41] have been focused on their strain energies, structures, aromaticities, band gaps, and reactivities. These studies reveal that the high chemical reactivity and highly strained structures of nanobelts underpin complications of their synthesis. Nevertheless, the development of new synthesis strategies[3,8,42−45] has allowed the achievement of the successful elusive synthesis[43] of a few nanobelts with distinct chemical structures.

The circular symmetry of nanorings, like CPPs, makes all electronic excited states fully delocalized across the entire molecule.[30] Because of this symmetry, the lowest nodeless electronic state S_1 is optically forbidden. Nevertheless, large CPPs are efficient emitters due to a spatial exciton localization (self-trapping) during photoinduced electronic energy relaxation. This self-trapping is attributed to dynamical dihedral rotations between phenyl units after photoexcitation.[33] On the contrary, carbon nanobelts are cylindrical molecules composed of fully fused edge-sharing arene rings. Therefore, their structural rigidity and strain of bonds prevent their deformation away from high symmetry, and thus, the excited state wave function is expected to remain delocalized. Within this context, it is interesting to understand how the high

Received: May 2, 2020
Accepted: May 28, 2020
Published: May 28, 2020

https://dx.doi.org/10.1021/acs.jpclett.0c01351
J. Phys. Chem. Lett. 2020, 11, 4711−4719

structural rigidity and wave function delocalization of nanobelts impact the photoinduced nonradiative relaxation processes that modulate their fluorescence yield.

Herein, we simulate the photoinduced dynamics of nanobelt **1** that has been successfully synthesized by Povie et al.[45] (see Figure 1a) using a nonadiabatic excited state molecular dynamics (NEXMD) framework.[46,47] Our NEXMD simulations uncover a critical role played by intermittent excited state wave function localization on the different types of carbon atoms, which controls the rate of internal conversion and creates bottlenecks in its time scales. Overall, the rigid structure of nanobelt **1** reveals a significantly slower electronic energy relaxation compared to that in carbon nanorings (e.g., CPPs) because of the reduced level of electron vibrational coupling.

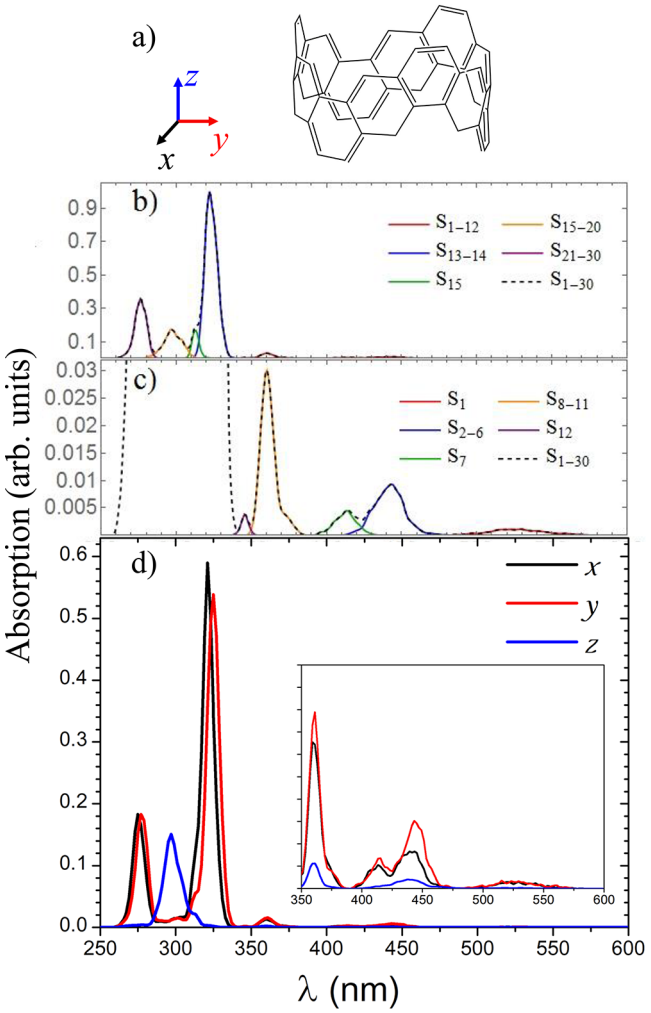

Figure 1. (a) Chemical structure of nanobelt **1**. The inertial *x*-, *y*-, and *z*-axes are also shown. (b) Calculated optical absorption spectrum at 300 K showing contributions from 30 individual excited states to the total spectrum. (c) Low-frequency range of the calculated absorption spectrum showing weak absorption features. (d) Relative absorbance intensities in the directions parallel to the inertial *x*-, *y*-, *z*-axes of nanobelt **1**.

We start with analysis of the excited structure in carbon nanobelt **1** shown in Figure 1a. Panels b and c of Figure 1 show its absorption spectra, obtained from vertical transition energies calculated for the collected initial structures equilibrated on the S_0 state at room temperature and weighted according to their corresponding oscillator strengths. The simulated spectrum captures the key features of the experimental spectrum given in parentheses:[45] (a) two major peaks at 275 (284) nm and 325 (313) nm, (b) a smaller peak localized at lower energies, ~360 (412) nm, and (c) a wider and less intensive band in the region between 500 and 550 nm attributed to the symmetry-forbidden S_1 state. Similar to CPP nanorings, the lowest S_1 state is nodeless and is delocalized across the entire molecule. Nevertheless, while in CPPs the main absorption peak is attributed to the strongly optically allowed degenerate S_2 and S_3 excited states,[30,33] the oscillator strengths of the 12 lowest excited states in the nanobelt remain relatively low. Here, the two main peaks at 275 and 325 nm correspond to contributions from states S_{13} and S_{14} and states S_{21-30}, respectively. The polarization of the different excitations is explored by translating and orienting each initially stored ground state configuration to a body fixed reference frame with the origin in their corresponding center of mass and their principal axes of rotation coincident with the Cartesian (x, y, z) coordinate axes. Therefore, the first and second moments of inertia are within the (x, y) plane of the nanobelt, and the third is oriented perpendicular to this plane (see Figure 1a). Within this new body fixed reference frame, we further calculate the transition dipole moments. Figure 1d shows the contributions of the different excited states to the resulting intensity of the polarized absorption spectra in the directions parallel to the inertial axes. We can observe that the transition dipole moments of most of the excited states are polarized in the (x, y) plane of the nanobelt. In contrast, the corresponding transitions to states $S_{16}-S_{19}$, localized between the two main peaks at 275 and 325 nm, are polarized along the *z*-axes. Therefore, a fast decay of the fluorescence anisotropy signal after initial laser excitation at 275 nm is predicted.

Photoinduced NEXMD simulations are started by vertical excitation at the 275 nm band according to the procedure described in *Simulation Details*. After photoexcitation, the internal conversion to the lowest-energy S_1 state is monitored by tracking the average populations of different electronic excited states as a function of time. This is shown in Figure 2. Excited states can be arranged in bands according to their energetics and similar behavior during the internal conversion process.

First, Figure 2a shows the band of states ($S_{21}-S_{30}$) that are initially populated by the laser according to their relative energies and oscillator strength as it is described in *Simulation Details*. These states form the major peak at 275 nm of the absorption spectrum (see Figure 1b). They experience an ultrafast depopulation by energy transfer to the band of states $S_{13}-S_{18}$ on an ~100 fs time scale. Despite S_{19} and S_{20} states not being initially populated by laser excitation, they are also included in the initial band due to their ultrafast relaxation rates comparable to that of the rest of the initial states. Actually, the high density of states in the range of approximately 260−290 nm contributes to a highly efficient population exchange and nonradiative relaxation.

Thereafter, the $S_{13}-S_{18}$ intermediate states, associated with the major band at 325 nm of the absorption spectrum, undergo similar population and depopulation (see Figure 2b). They all transiently acquire an excess of energy by ~100 fs with the S_{13} state attaining the largest population. This behavior is a consequence of the energy gap between states S_{12} and S_{13},

https://dx.doi.org/10.1021/acs.jpclett.0c01351
J. Phys. Chem. Lett. 2020, 11, 4711−4719

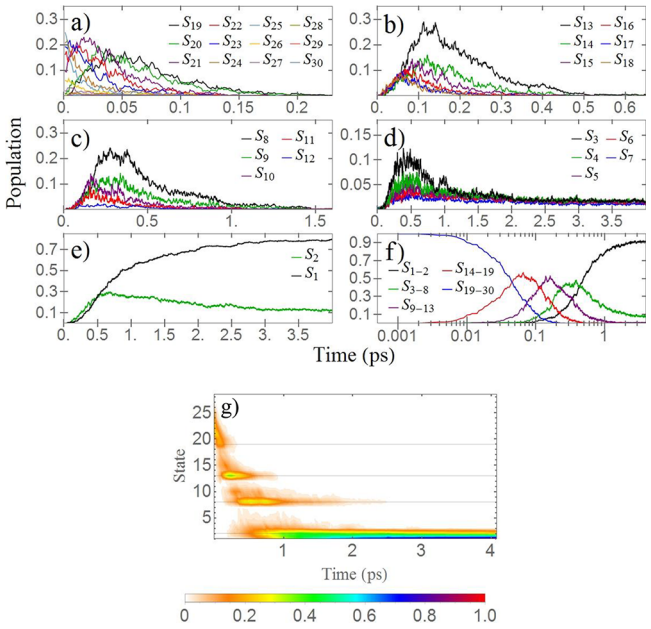

Figure 2. (a–e) Evolution over time of electronic state populations for different bands of states. (f) Evolution over time of populations associated with these bands plotted on a logarithmic time scale. (g) Evolution over time of the probability density of the current state. Thin horizontal lines indicate long-lived excited states presenting bottlenecks of nonradiative relaxation.

shown in Figure 1b. Subsequently, S_{13} is a relatively long-lived intermediate state decaying on an ∼500 fs time scale.

The third band of states, shown in Figure 2c, is comprised of states S_8–S_{12}. It involves the shoulder in the absorption spectrum appearing at lower energies (∼360 nm). Here, state S_8 transiently acquires the largest population and holds it for a longer time of ≲1 ps. This state has a significant energy gap with state S_7, and therefore, its relaxation is slower compared to that of the other states. Finally, the fourth band is formed by states S_3–S_7 (see Figure 2d). They relax to state S_2 on ∼1 ps time scales that ultimately further transfers its population to state S_1 (Figure 2e) during several picoseconds.

To further validate our simulations with respect to experimental measurements, the emission spectrum has been obtained from vertical transition energies calculated for the collected set of final structures and weighted according to their S_1 oscillator strengths. (see Figure S1). Despite the fact that the last time of our simulations was only 4 ps, we observed a broad emission band extending to a near-infrared region with a maximum emission at ∼610 nm, in excellent agreement with the broad band at 630 nm reported experimentally.[45]

The overall relaxation process described above can be pictorially shown in the contour plot in Figure 2g that depicts the evolution over time of the probability density of the current state, that is, the state that dictates the nuclear motion according to the FSSH approach. Following photoexcitation, the presence of four long-lived excited states (S_2, S_8, S_{13}, and S_{19}), which are separated from the lower-energy states by large energy gaps (see Figure 1b,c), creates bottlenecks in the sequential relaxation process across an otherwise dense manifold of excited states. We quantified the excitation (τ_{exc}) and relaxation (τ_{rel}) times for bottleneck states by fitting the population curves with exponential growth and decay functions of the form $f(t) = 1 - A\exp\left(-\frac{t}{\tau_{exc}}\right)$ and $f(t) = A\exp\left(-\frac{t}{\tau_{rel}}\right)$, respectively. The values of τ_{exc} and τ_{rel} are 36 and 58 fs, 37 and 116 fs, and 160 and 1539 fs for long-lived intermediate states S_{19}, S_{13}, and S_8, respectively. That is, as the energy relaxation to the final S_1 state progresses, we observe an increase in the difference between the rate at which these states receive population from the high-energy states and the rate at which they are depopulated. As a consequence, Figure 2g shows that these intermediate bottleneck states have increasingly larger lifetimes with a decrease energy. Notably, Figure 2f shows the evolution over time of each bundle of states using a logarithmic time scale. The Gaussian shapes for each bundle of states indicate that they relax with rates that are much slower than those that are excited. The similarity between the Gaussians indicates that this slowdown seems to occur in a similar manner for each bundle. Furthermore, the equivalent Gaussian heights indicate that the three bands considered transiently acquire equivalent quantities of populations.

At this point, it is worth mentioning that the nonradiative relaxation of nanobelt **1** is significantly slower compared to previously reported internal conversion time scales in CPPs that usually reaches completion within hundreds of femtoseconds.[33] The structural rigidity of nanobelt **1** ensures the high-symmetry geometry with minimal conformational dynamics. Therefore, exciton self-trapping due to structural disorder introduced by vibrational couplings and thermal fluctuations should be limited in the nanobelt due to its high strain. To analyze this feature, Figure 3a displays the time

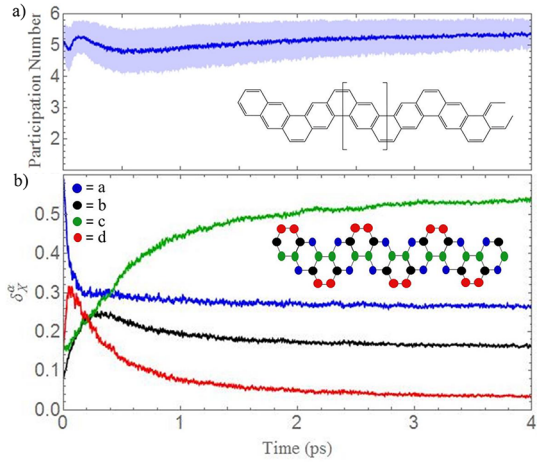

Figure 3. (a) Evolution over time of the participation number $PN(t)$ with $\delta_X^\alpha(t)$ defined as the transition density localized on each of the six fragments shown between brackets in the extended scheme of the nanobelt **1** shown in the inset. (b) Evolution over time of the electronic transition density decomposed in contributions $\delta_X^\alpha(t)$ from the four different types of atoms defined in the extended scheme of nanobelt **1** shown in the inset.

evolution of the participation number $PN(t)$ (see eq 3), with $\delta_X^\alpha(t)$ defined as the transition density localized on each of the six fragments shown between brackets in the extended scheme of nanobelt **1** displayed in the inset. We can observe that the electronic transition density remains always strongly delocalized across the entire nanobelt. Previous works performed on [*n*]CPPs of different sizes[30,33] (n = 9–16) have shown that the exciton becomes localized on only five phenyl rings within 50 fs after excitation, the effect being more pronounced in larger

https://dx.doi.org/10.1021/acs.jpclett.0c01351
J. Phys. Chem. Lett. 2020, 11, 4711–4719

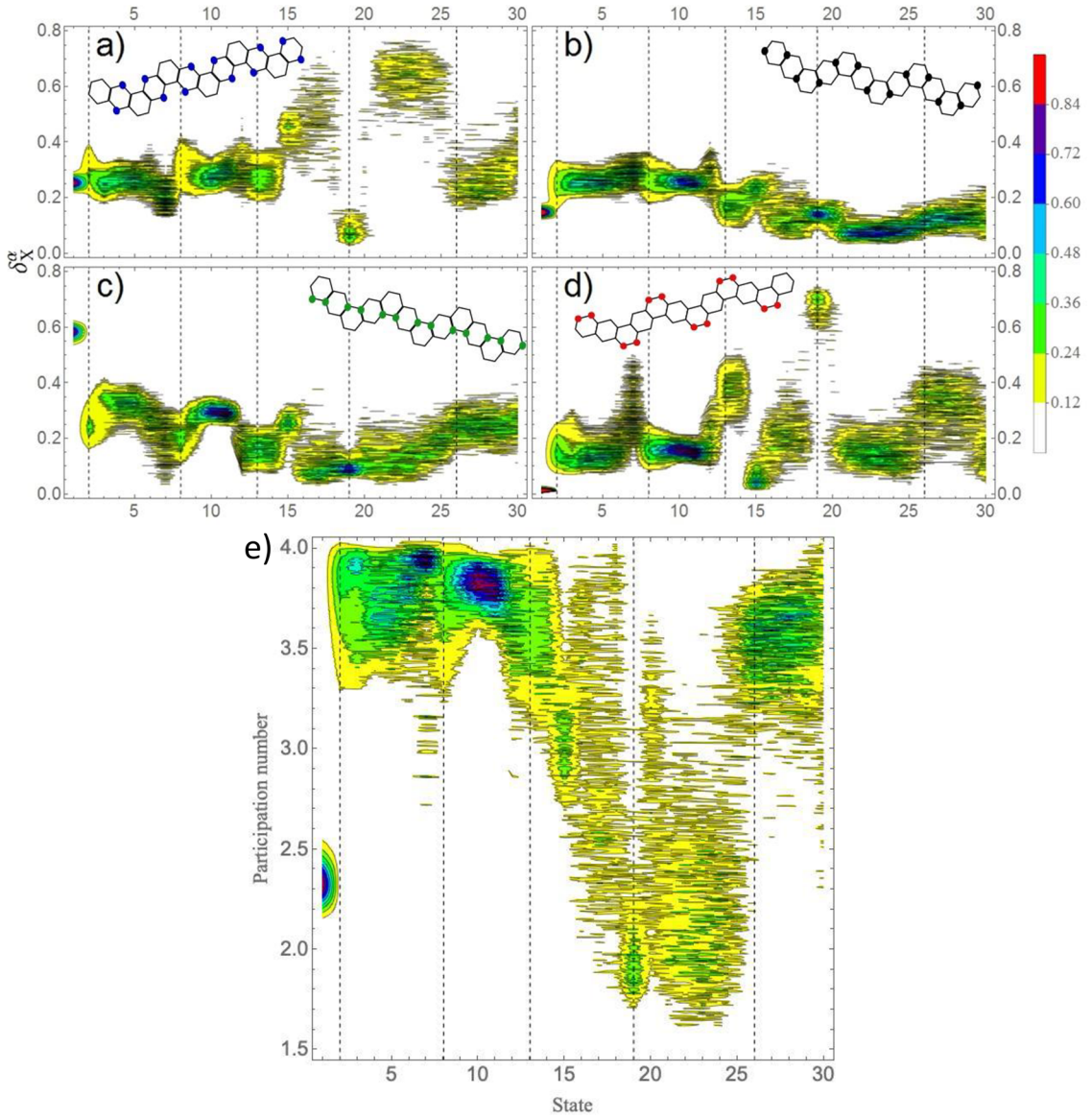

Figure 4. (a–d) Probability density of the fraction of transition density $\delta_X^\alpha(t)$ on each type of atom for the different excited states at times when they correspond to the current state during the internal conversion. (e) Probability density of the participation number PN(t) with $\delta_X^\alpha(t)$ defined as the transition density localized on each of the four types of atoms. Long-lived excited states S_2, S_8, S_{13}, and S_{19} are indicated by vertical dashed lines.

systems. This exciton self-trapping does not takes place in nanobelt **1**. This is in good agreement with previous time-resolved measurements[45] that have reported rates of radiative decay in accord with a forbidden transition associated with a nodeless S_1 state delocalized across the entire molecule.

A further characterization of the internal conversion of nanobelt **1** can be achieved by decomposing the electronic transition density into contributions $\delta_X^\alpha(t)$ from the four different types of carbon atoms defined in the extended scheme of nanobelt **1** shown in Figure 3b. The photoexcitation centered at the 275 nm band of the absorption spectra has a predominant contribution from the *a* type of atom. After transiently passing through the *d* and *b* types of atoms, it finishes by being mainly localized on the *c* atoms.

The intramolecular energy redistribution among the different types of atoms can be related to the passage of the photoexcited wavepacket through the dense manifold of excited states during the internal conversion process that heads to the lowest state S_1. This is analyzed in panels a–d of Figure 4 that show the probability density of the fraction of transition density, $\delta_X^\alpha(t)$, on each X = *a*, *b*, *c*, or *d* type of atom for the different excited states during the internal conversion process. We observe that the first S_{20}–S_{25} band centered at the 275 nm peak in the absorption spectra is mainly localized on the *a* atoms (Figure 4a). The passage through the long-lived S_{19} state represents a significant change in the exciton localization because S_{19} is mainly localized on the *d* atoms (Figure 4d). S_{19} seems to be the only state localized on the *d* atoms in this energy region because low-lying excited states S_{15}–S_{18} are again essentially centered on *a* atoms (Figure 4a). These sudden changes in localization involving the long-lived S_{19} state reduce the wave function overlap with neighboring states and, therefore, the corresponding nonadiabatic couplings. Moreover, the transient ultrafast accumulation of $\delta_d^\alpha(t)$, observed in Figure 3b, can be related to the transient increase in the population of this state that contributes to the absorption polarization along the *z*-axes (see Figure 1d), because the *d* atoms are the ones that contribute the most to

https://dx.doi.org/10.1021/acs.jpclett.0c01351
J. Phys. Chem. Lett. 2020, 11, 4711–4719

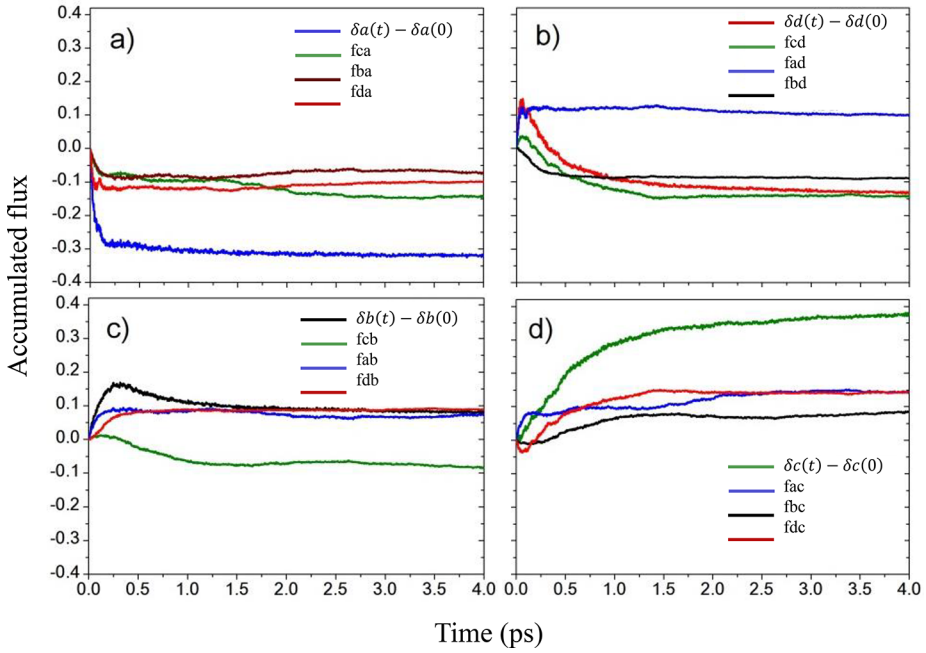

Figure 5. Accumulated fluxes between the different types of atoms using the transition density flux analysis. The types of atom are defined in Figure 3b.

an increase in the intensity of the polarized absorption in this direction.

The passage of the molecular system through states S_{13} and S_{14} associated with the major 325 nm absorption peak represents a transient exciton delocalization involving all atom types. The passage through long-lived state S_8 also represents an exciton intramolecular redistribution with a transient increase in the localization on *d* atoms (Figure 4d). Again, these significant differences in the exciton localization for this state compared with the localization for its neighbor's states reduce the corresponding nonadiabatic couplings and, therefore, accentuate the role of S_8 as a bottleneck state. Finally, while states S_2-S_7 correspond to a delocalized exciton, the final energy transfer to state S_1 involves a sudden change in the exciton localization to the *c* type of atoms. The average fractions of the transition density of S_1 localized on the *c* type of atoms at the initial moment of photoexcitation and at the end of the internal conversion process are 0.55 ± 0.03 and 0.58 ± 0.02, respectively. That is, the excited state dynamics does not change noticeably localization of S_1 on *c* atoms compared to the localization expected from the ensemble of equilibrated configurations at S_0. This is expected due to the high structural rigidity of nanobelt **1** that prevents significant geometry deformations. Figure S2 displays snapshots of the transition density during transient population of different excited states for an individual NEXMD trajectory.

Changes in the spatial evolution of the electronic transition density during the internal conversion process can also be rationalized by analyzing the participation number PN(t) (see eq 3), with $\delta_X^\alpha(t)$ defined as the transition density localized on each of the four types of atoms. That is, PN(t) varies in the range of 1−4. PN(t) values of ≈1 indicate a complete localization of $\delta_X^\alpha(t)$ on a unique type of atom, while PN(t) values of ≈4 indicate a complete exciton spreading over all types of atoms.

For each state, the excited state distribution of PN(t) is constructed by collecting excited state geometries during NEXMD at all times for which the electronic state of interest corresponds to the current state; that is, it defines the nuclear propagation according to the FSSH approach. The probability density of values of PN(t) by state is displayed in Figure 4e. We can observe sudden changes in the exciton localization/delocalization among the different types of atoms close to the long-lived states. High-energy states, involving the two main bands at 275 and 325 nm of the absorption spectrum, are more localized on specific types of atoms compared to that of the lower-energy states. As an exception, we observed that the S_2-S_1 energy transfer involves an abrupt localization of the exciton in terms of atom types.

Further details about the electronic energy relaxation process can be obtained using the transition density flux analysis described in *Simulation Details*. Figure 5 shows the evolution over time of the accumulated transition densities $\delta_X(t) - \delta_X(0)$ for the different X types of atoms in addition to the respective fluxes $f_{XY}(t)$. Figure 5a indicates that the initial exciton localization on the *a* atoms is rapidly transferred to the other types. While *d* atoms are initially the main acceptors, the $a \rightarrow c$ flux increases at longer times. In addition, there is also a minor flux to *b* atoms. After that, Figure 5b shows that *d* atoms transfer their excitation mainly to *c* atoms along with a minor flux to *b* atoms. These minor fluxes to *b* atoms are subsequently being rerouted to *c* atoms (see Figure 5c), so that the progressive exciton localization on the *c* atoms during the electronic energy relaxation is due to an exciton redistribution from the other three types of atoms through the main relaxation $a \rightarrow d \rightarrow c$ and $a \rightarrow c$ pathways with some minor contributions from $a \rightarrow d \rightarrow b \rightarrow c$ and $a \rightarrow b \rightarrow c$ pathways.

The photoinduced electronic energy relaxation and redistribution of the fully fused edge-sharing carbon nanobelt **1** have been simulated using nonadiabatic excited state molecular dynamics. The structural rigidity of nanobelt **1** prevents deformation of high-symmetry geometry due to reduced election vibrational coupling and minimal effects of thermal

https://dx.doi.org/10.1021/acs.jpclett.0c01351
J. Phys. Chem. Lett. 2020, 11, 4711−4719

fluctuations. Therefore, the electronic transition density for all excited states remains always delocalized, and exciton self-trapping, previously reported during photoinduced processes of nanorings (e.g., CPPs), is not observed. Moreover, the nonradiative relaxation process occurs on several picosecond time scales and is ∼1 order of magnitude slower compared to that in CPPs (the latter according to previous reports that take place at a time scale of hundreds of femtoseconds).

After photoexcitation of nanobelt **1**, the internal conversion samples the dense manifold of excited states, which can be bundled into bands of states featuring similar transient population and depopulation dynamics. These bands relax consecutively slower compared to the rate of their excitation. This slowdown seems to occur at a similar degree for each band. Therefore, these bands of states transiently acquire similar quantities of populations, and their relaxation rate decreases with a decrease in energy.

Observed bands of states are separated by the long-lived excited states at the edge of large energy gaps with the lower-energy states, creating vibrational bottlenecks in the electronic relaxation. Moreover, the passage of the photoexcited wave-packet through these long-lived states involves significant changes in the exciton wave function spatial localization and delocalization involving different types of carbon atoms that compose the nanobelt. Our analysis of excited state transition density behavior exposes different types of carbon atoms critically affecting the internal conversion process. As such, we are able to describe in detail the excited state dynamics and the exciton redistribution through portions of the nanobelt scaffold. These peculiarities of excited state dynamics suggest synthetic means, like complexation with a variety of guests in a supramolecular chemistry, to control internal conversion rates in this molecular family. These insights could be valuable for tuning the nanobelt structures for specific nanoelectronic and photonic applications.

NEXMD Overview. The NEXMD computational package[46,47] makes use of the fewest switching surface hopping (FSSH) algorithm[48,49] to simulate the photoinduced nonradiative electronic and vibrational relaxation of large molecular systems going through several coupled electronic excited states. Excited state energies,[50−52] gradients,[53,54] and nonadiabatic couplings[46,55−57] are calculated "on the fly" at the configuration interaction single (CIS) level of theory using the semiempirical Austin model 1 Hamiltonian[58] by means of the Collective Electronic Oscillator (CEO) approach.[59−61] This methodology has been described in detail elsewhere.[47]

Spatial Excitonic Localization and Dynamics. The CEO approach calculates transition density matrices whose elements can be written as[62,63]

$$(\rho^{g\alpha})_{nm} = \langle \phi_\alpha | c_m^\dagger c_n | \phi_g \rangle \tag{1}$$

where ϕ_g and ϕ_α represent the CIS adiabatic ground and excited state wave functions, respectively, and $c_m^\dagger$ and c_n are the creation and annihilation operators of electrons for atomic orbitals (AO) m and n, respectively. Diagonal elements represent the changes in the distribution of electronic density on the mth AO induced by the photoexcitation from the ground state to the singlet excited state S_α.[62,64] This feature makes them useful for tracking the relaxation dynamics of the excited state wave functions in real space.

According to the normalization condition $\sum_{n,m}[\rho_{nm}^{g\alpha}(t)]^2 = 1$,[52] the fraction of the transition density localized on each specific fragment or type of atom of the nanobelt is obtained as

$$\delta_X^\alpha(t) = [\rho^{g\alpha}(t)]_X^2 = \sum_{n_A m_A} [\rho^{g\alpha}(t)]_{n_A m_A}^2 \tag{2}$$

where index A runs over all atoms localized in the fragment or type of atom X. To measure the extent of (de)localization of $\delta_X^\alpha(t)$ among the fragments or the different type of atoms, we define the participation number as[65,66]

$$\mathrm{PN}(t) = \left\{ \sum_X [\delta_X^\alpha(t)]^2 \right\}^{-1} \tag{3}$$

$\mathrm{PN}(t)$ values of ≈1 indicate a complete localization of $\delta_X^\alpha(t)$ on a single fragment or type of atom, while $\mathrm{PN}(t)$ values of ≈N, N being the total number of fragments or type of atoms in the nanobelt, correspond to $\delta_X^\alpha(t)$ fully delocalized across the molecule. Herein, we use $\mathrm{PN}(t)$ in two different manners. First, we use it to evaluate the degree of exciton delocalization among the six equivalent fragments shown between brackets in the extended scheme of the nanobelt 1 shown as the inset in Figure 3a. Therefore, the summation in eq 2 is performed over atomic orbitals localized on each of these six equivalent fragments, and the value of $\mathrm{PN}(t)$ varies between 1 (i.e., the exciton completely localized on one fragment) and 6 (i.e., the exciton completely delocalized on the whole nanobelt). Second, we use it to evaluate the degree of exciton delocalization among the four types of atoms indicated in Figure 3b. Therefore, the summation in eq 2 is performed over atomic orbitals localized on atoms that belong to each of these types, and the $\mathrm{PN}(t)$ value varies between 1 (i.e., the exciton completely localized on one type of atom) and 4 (i.e., the exciton sparsed among any kind of atom).

The flux of $\delta_X^\alpha(t)$, subsequent to the initial photoexcitation of the nanobelt, is monitored by applying the transition density flux analysis,[67] originally developed to analyze the vibrational energy flow in polyatomic molecules.[68] Herein, we briefly summarize the method. The effective change in $\delta_X^\alpha(t)$ [$\Delta\delta_X(t)$, where the superindex indicating the current state α for the NEXMD propagation has been omitted] is monitored by analyzing flow matrix $F(t)$ between the consecutive times at each time step Δt throughout NEXMD simulations. $F(t)$ has vanishing diagonal elements, and off-diagonal elements $f_{XY}(t)$ contain the amount of $\delta_X(t)$ transferred between molecular fragments (or types of atom) X and Y. We classify X and Y as donors (D) if $\delta_X(t) < 0$ or acceptors (A) if $\delta_X(t) > 0$ by imposing the minimum flow criterion. That assumes that the amount of $\Delta\delta_X(t)$ is a minimum. That is, only effective $\delta_X(t)$ flows from D to A are considered. The total transition density exchanged among units during each Δt is

$$\Delta\delta_{\mathrm{total}}(t) = \sum_{X\in D} \left| \Delta\delta_X(t) \right| = \sum_{X\in A} \Delta\delta_Y(t) \tag{4}$$

And elements $f_{XY}(t)$ are calculated as

$$f_{XY}(t) = -f_{YX}(t) = \begin{cases} \dfrac{|\Delta\delta_X(t)|\Delta\delta_Y(t)}{\Delta\delta_{\mathrm{total}}(t)} & X \in D,\ Y \in A \\ 0 & X, Y \in D \text{ or } X, Y \in A \end{cases} \tag{5}$$

A detailed derivation of eq 5 can be found elsewhere.[67]

https://dx.doi.org/10.1021/acs.jpclett.0c01351
J. Phys. Chem. Lett. 2020, 11, 4711−4719

Simulation Details. NEXMD simulations were performed on nanobelt **1** shown in Figure 1a. The initial conditions for each photoinduced NEXMD trajectory were selected as follows. The initial positions and momenta of the nuclei (i.e., conformational snapshots) were obtained from 1000 samples collected from a 1 ns equilibrated ground state (S_0) molecular dynamics simulation with the system equilibrated at room (300 K) temperature using the Langevin thermostat[69,70] with a friction coefficient of 20 ps^{-1}. A Franck−Condon window given by the equation $g_\alpha = \exp[-T^2(E_{laser} - \Omega_\alpha)^2]$ was used. Ω_α and E_{laser} represent the energy of the αth excited state and the energy of a Gaussian laser pulse $f(t) = \exp\left(-\frac{t^2}{2T^2}\right)$ centered at 275 nm, respectively. A T^2 value of 42.5 fs, corresponding to a full width at half-maximum of 100 fs, was considered. Finally, the initial excited state is selected randomly according to the relative values of g_α weighted by the oscillator strengths of each α state.

Thirty singlet electronic excited states and their corresponding nonadiabatic couplings were included. NEXMD simulations were performed at a constant energy. Classical time steps of 0.5 and 0.1 fs have been used for the propagation of nuclei in ground state and photoinduced simulations, respectively. In addition, a quantum time step of 0.025 fs has been used to propagate the electronic degrees of freedom. Corrections for decoherence[71] and trivial unavoided crossings[72,73] were included, as well. Parameters and the methodology of NEXMD simulations have been extensively discussed elsewhere.[47,74]

■ ASSOCIATED CONTENT

Supporting Information

The Supporting Information is available free of charge at https://pubs.acs.org/doi/10.1021/acs.jpclett.0c01351.

Calculated optical emission spectrum of nanobelt **1** at 300 K and snapshots of the transition density during transient population of different excited states for an individual NEXMD trajectory (PDF)

■ AUTHOR INFORMATION

Corresponding Author

S. Fernandez-Alberti − *Departamento de Ciencia y Tecnologia, Universidad Nacional de Quilmes/CONICET, B1876BXD Bernal, Argentina;* orcid.org/0000-0002-0916-5069; Email: sfalberti@gmail.com

Authors

V. M. Freixas − *Departamento de Ciencia y Tecnologia, Universidad Nacional de Quilmes/CONICET, B1876BXD Bernal, Argentina;* orcid.org/0000-0003-1733-4827

N. Oldani − *Departamento de Ciencia y Tecnologia, Universidad Nacional de Quilmes/CONICET, B1876BXD Bernal, Argentina*

R. Franklin-Mergarejo − *Departamento de Ciencia y Tecnologia, Universidad Nacional de Quilmes/CONICET, B1876BXD Bernal, Argentina*

S. Tretiak − *Theoretical Division, Center for Nonlinear Studies (CNLS), and Center for Integrated Nanotechnologies (CINT), Los Alamos National Laboratory, Los Alamos, New Mexico 87545, United States;* orcid.org/0000-0001-5547-3647

Complete contact information is available at: https://pubs.acs.org/10.1021/acs.jpclett.0c01351

Notes

The authors declare no competing financial interest.

■ ACKNOWLEDGMENTS

This work was performed in part at the Center for Nonlinear Studies (CNLS) and the Center for Integrated Nanotechnology (CINT), a U.S. Department of Energy and Office of Basic Energy Sciences user facility. The authors acknowledge support from the Los Alamos National Laboratory (LANL) Directed Research and Development funds (LDRD). This research used resources provided by the LANL Institutional Computing Program. S.F.-A., N.O, R. F-M., and V.M.F. acknowledge the support of CONICET, UNQ, and ANPCyT (PICT-2018-02360).

■ REFERENCES

(1) Jasti, R.; Bertozzi, C. R. Progress and Challenges for the Bottom-up Synthesis of Carbon Nanotubes with Discrete Chirality. *Chem. Phys. Lett.* **2010**, *494*, 1−7.

(2) Steinberg, B. D.; Scott, L. T. New Strategies for Synthesizing Short Sections of Carbon Nanotubes. *Angew. Chem., Int. Ed.* **2009**, *48*, 5400−5402.

(3) Gleiter, R.; Esser, B.; Kornmayer, S. C. Cyclacenes: Hoop-Shaped Systems Composed of Conjugated Rings. *Acc. Chem. Res.* **2009**, *42*, 1108−1116.

(4) Omachi, H.; Nakayama, T.; Takahashi, E.; Segawa, Y.; Itami, K. Initiation of Carbon Nanotube Growth by Well-Defined Carbon Nanorings. *Nat. Chem.* **2013**, *5*, 572−576.

(5) Omachi, H.; Segawa, Y.; Itami, K. Synthesis and Racemization Process of Chiral Carbon Nanorings: A Step toward the Chemical Synthesis of Chiral Carbon Nanotubes. *Org. Lett.* **2011**, *13*, 2480−2483.

(6) Bodwell, G. J. Growth Potential. *Nat. Nanotechnol.* **2010**, *5*, 103−104.

(7) Iyoda, M.; Yamakawa, J.; Rahman, M. J. Conjugated Macrocycles: Concepts and Applications. *Angew. Chem., Int. Ed.* **2011**, *50*, 10522−10553.

(8) Kawase, T.; Kurata, H. Ball-, Bowl-, and Belt-Shaped Conjugated Systems and Their Complexing Abilities: Exploration of the Concave−Convex Π−π Interaction. *Chem. Rev.* **2006**, *106*, 5250−5273.

(9) Iwamoto, T.; Watanabe, Y.; Sadahiro, T.; Haino, T.; Yamago, S. Size-Selective Encapsulation of C60 by [10]Cycloparaphenylene: Formation of the Shortest Fullerene-Peapod. *Angew. Chem., Int. Ed.* **2011**, *50*, 8342−8344.

(10) Xia, J.; Bacon, J. W.; Jasti, R. Gram-Scale Synthesis and Crystal Structures of [8]- and [10]CPP, and the Solid-State Structure of C60@[10]CPP. *Chem. Sci.* **2012**, *3*, 3018.

(11) Iwamoto, T.; Watanabe, Y.; Takaya, H.; Haino, T.; Yasuda, N.; Yamago, S. Size- and Orientation-Selective Encapsulation of C 70 by Cycloparaphenylenes. *Chem. - Eur. J.* **2013**, *19*, 14061−14068.

(12) Iwamoto, T.; Slanina, Z.; Mizorogi, N.; Guo, J.; Akasaka, T.; Nagase, S.; Takaya, H.; Yasuda, N.; Kato, T.; Yamago, S. Partial Charge Transfer in the Shortest Possible Metallofullerene Peapod, La@C 82 ⊂[11]Cycloparaphenylene. *Chem. - Eur. J.* **2014**, *20*, 14403−14409.

(13) Ueno, H.; Nishihara, T.; Segawa, Y.; Itami, K. Cycloparaphenylene-Based Ionic Donor-Acceptor Supramolecule: Isolation and Characterization of Li + @C 60 ⊂[10]CPP. *Angew. Chem., Int. Ed.* **2015**, *54*, 3707−3711.

(14) Leonhardt, E. J.; Jasti, R. Emerging Applications of Carbon Nanohoops. *Nat. Rev. Chem.* **2019**, *3*, 672−686.

(15) Kim, P.; Park, K. H.; Kim, W.; Tamachi, T.; Iyoda, M.; Kim, D. Relationship between Dynamic Planarization Processes and Exciton Delocalization in Cyclic Oligothiophenes. *J. Phys. Chem. Lett.* **2015**, *6*, 451−456.

(16) Peña-Alvarez, M.; Qiu, L.; Taravillo, M.; Baonza, V. G.; Delgado, M. C. R.; Yamago, S.; Jasti, R.; Navarrete, J. T. L.; Casado, J.; Kertesz, M. From Linear to Cyclic Oligoparaphenylenes: Electronic and Molecular Changes Traced in the Vibrational Raman Spectra and Reformulation of the Bond Length Alternation Pattern. *Phys. Chem. Chem. Phys.* **2016**, *18*, 11683−11692.
(17) Segawa, Y.; Yagi, A.; Ito, H.; Itami, K. A Theoretical Study on the Strain Energy of Carbon Nanobelts. *Org. Lett.* **2016**, *18*, 1430−1433.
(18) Lewis, S. E. Cycloparaphenylenes and Related Nanohoops. *Chem. Soc. Rev.* **2015**, *44*, 2221−2304.
(19) Segawa, Y.; Miyamoto, S.; Omachi, H.; Matsuura, S.; Šenel, P.; Sasamori, T.; Tokitoh, N.; Itami, K. Concise Synthesis and Crystal Structure of [12]Cycloparaphenylene. *Angew. Chem., Int. Ed.* **2011**, *50*, 3244−3248.
(20) Segawa, Y.; Fukazawa, A.; Matsuura, S.; Omachi, H.; Yamaguchi, S.; Irle, S.; Itami, K. Combined Experimental and Theoretical Studies on the Photophysical Properties of Cycloparaphenylenes. *Org. Biomol. Chem.* **2012**, *10*, 5979.
(21) Hirst, E. S.; Jasti, R. Bending Benzene: Syntheses of [n]Cycloparaphenylenes. *J. Org. Chem.* **2012**, *77*, 10473−10478.
(22) Li, P.; Sisto, T. J.; Darzi, E. R.; Jasti, R. The Effects of Cyclic Conjugation and Bending on the Optoelectronic Properties of Paraphenylenes. *Org. Lett.* **2014**, *16*, 182−185.
(23) Chen, H.; Golder, M. R.; Wang, F.; Jasti, R.; Swan, A. K. Raman Spectroscopy of Carbon Nanohoops. *Carbon* **2014**, *67*, 203−213.
(24) Nishihara, T.; Segawa, Y.; Itami, K.; Kanemitsu, Y. Excited States in Cycloparaphenylenes: Dependence of Optical Properties on Ring Length. *J. Phys. Chem. Lett.* **2012**, *3*, 3125−3128.
(25) Fujitsuka, M.; Cho, D. W.; Iwamoto, T.; Yamago, S.; Majima, T. Size-Dependent Fluorescence Properties of [n]-Cycloparaphenylenes (n = 8−13), Hoop-Shaped π-Conjugated Molecules. *Phys. Chem. Chem. Phys.* **2012**, *14*, 14585.
(26) Zabula, A. V.; Filatov, A. S.; Xia, J.; Jasti, R.; Petrukhina, M. A. Tightening of the Nanobelt upon Multielectron Reduction. *Angew. Chem., Int. Ed.* **2013**, *52*, 5033−5036.
(27) Iwamoto, T.; Watanabe, Y.; Sakamoto, Y.; Suzuki, T.; Yamago, S. Selective and Random Syntheses of [n]Cycloparaphenylenes (n = 8−13) and Size Dependence of Their Electronic Properties. *J. Am. Chem. Soc.* **2011**, *133*, 8354−8361.
(28) Segawa, Y.; Omachi, H.; Itami, K. Theoretical Studies on the Structures and Strain Energies of Cycloparaphenylenes. *Org. Lett.* **2010**, *12*, 2262−2265.
(29) Sundholm, D.; Taubert, S.; Pichierri, F. Calculation of Absorption and Emission Spectra of [n]Cycloparaphenylenes: The Reason for the Large Stokes Shift. *Phys. Chem. Chem. Phys.* **2010**, *12*, 2751.
(30) Adamska, L.; Nayyar, I.; Chen, H.; Swan, A. K.; Oldani, N.; Fernandez-Alberti, S.; Golder, M. R.; Jasti, R.; Doorn, S. K.; Tretiak, S. Self-Trapping of Excitons, Violation of Condon Approximation, and Efficient Fluorescence in Conjugated Cycloparaphenylenes. *Nano Lett.* **2014**, *14*, 6539−6546.
(31) Wong, B. M. Optoelectronic Properties of Carbon Nanorings: Excitonic Effects from Time-Dependent Density Functional Theory. *J. Phys. Chem. C* **2009**, *113*, 21921−21927.
(32) Camacho, C.; Niehaus, T. A.; Itami, K.; Irle, S. Origin of the Size-Dependent Fluorescence Blueshift in [n]Cycloparaphenylenes. *Chem. Sci.* **2013**, *4*, 187−195.
(33) Oldani, N.; Doorn, S. K.; Tretiak, S.; Fernandez-Alberti, S. Photoinduced Dynamics in Cycloparaphenylenes: Planarization, Electron−Phonon Coupling, Localization and Intra-Ring Migration of the Electronic Excitation. *Phys. Chem. Chem. Phys.* **2017**, *19*, 30914−30924.
(34) Friederich, R.; Nieger, M.; Vögtle, F. Auf Dem Weg Zu Makrocyclischenpara-Phenylenen. *Chem. Ber.* **1993**, *126*, 1723−1732.
(35) Jasti, R.; Bhattacharjee, J.; Neaton, J. B.; Bertozzi, C. R. Synthesis, Characterization, and Theory of [9]-, [12]-, and [18]-Cycloparaphenylene: Carbon Nanohoop Structures. *J. Am. Chem. Soc.* **2008**, *130*, 17646−17647.
(36) Evans, P. J.; Darzi, E. R.; Jasti, R. Efficient Room-Temperature Synthesis of a Highly Strained Carbon Nanohoop Fragment of Buckminsterfullerene. *Nat. Chem.* **2014**, *6*, 404−408.
(37) Darzi, E. R.; Sisto, T. J.; Jasti, R. Selective Syntheses of [7]−[12]Cycloparaphenylenes Using Orthogonal Suzuki−Miyaura Cross-Coupling Reactions. *J. Org. Chem.* **2012**, *77*, 6624−6628.
(38) Evans, P. J.; Jasti, R. *Molecular Belts; Polyarenes I*; Springer: Berlin, 2012; pp 249−290.
(39) Sisto, T. J.; Golder, M. R.; Hirst, E. S.; Jasti, R. Selective Synthesis of Strained [7]Cycloparaphenylene: An Orange-Emitting Fluorophore. *J. Am. Chem. Soc.* **2011**, *133*, 15800−15802.
(40) Chen, Z.; Jiang, D.; Lu, X.; Bettinger, H. F.; Dai, S.; Schleyer, P. v. R.; Houk, K. N. Open-Shell Singlet Character of Cyclacenes and Short Zigzag Nanotubes. *Org. Lett.* **2007**, *9*, 5449−5452.
(41) Hirst, E. S.; Wang, F.; Jasti, R. Theoretical Analysis of [5.7] n Cyclacenes: Closed-Shell Cyclacene Isomers. *Org. Lett.* **2011**, *13*, 6220−6223.
(42) Tahara, K.; Tobe, Y. Molecular Loops and Belts. *Chem. Rev.* **2006**, *106*, 5274−5290.
(43) Eisenberg, D.; Shenhar, R.; Rabinovitz, M. Synthetic Approaches to Aromatic Belts: Building up Strain in Macrocyclic Polyarenes. *Chem. Soc. Rev.* **2010**, *39*, 2879.
(44) Yagi, A.; Segawa, Y.; Itami, K. Synthesis and Properties of [9]Cyclo-1,4-Naphthylene: A π-Extended Carbon Nanoring. *J. Am. Chem. Soc.* **2012**, *134*, 2962−2965.
(45) Povie, G.; Segawa, Y.; Nishihara, T.; Miyauchi, Y.; Itami, K. Synthesis of a Carbon Nanobelt. *Science* **2017**, *356*, 172−175.
(46) Nelson, T.; Fernandez-Alberti, S.; Roitberg, A. E.; Tretiak, S. Nonadiabatic Excited-State Molecular Dynamics: Modeling Photophysics in Organic Conjugated Materials. *Acc. Chem. Res.* **2014**, *47*, 1155−1164.
(47) Nelson, T. R.; White, A. J.; Bjorgaard, J. A.; Sifain, A. E.; Zhang, Y.; Nebgen, B.; Fernandez-Alberti, S.; Mozyrsky, D.; Roitberg, A. E.; Tretiak, S. Non-Adiabatic Excited-State Molecular Dynamics: Theory and Applications for Modeling Photophysics in Extended Molecular Materials. *Chem. Rev.* **2020**, *120*, 2215−2287.
(48) Tully, J. C. Molecular Dynamics with Electronic Transitions. *J. Chem. Phys.* **1990**, *93*, 1061−1071.
(49) Hammes-Schiffer, S.; Tully, J. C. Proton Transfer in Solution: Molecular Dynamics with Quantum Transitions. *J. Chem. Phys.* **1994**, *101*, 4657−4667.
(50) Tretiak, S.; Mukamel, S. Density Matrix Analysis and Simulation of Electronic Excitations in Conjugated and Aggregated Molecules. *Chem. Rev.* **2002**, *102*, 3171−3212.
(51) Chernyak, V.; Schulz, M. F.; Mukamel, S.; Tretiak, S.; Tsiper, E. V. Krylov-Space Algorithms for Time-Dependent Hartree−Fock and Density Functional Computations. *J. Chem. Phys.* **2000**, *113*, 36−43.
(52) Tretiak, S.; Isborn, C. M.; Niklasson, A. M. N.; Challacombe, M. Representation Independent Algorithms for Molecular Response Calculations in Time-Dependent Self-Consistent Field Theories. *J. Chem. Phys.* **2009**, *130*, No. 054111.
(53) Furche, F.; Ahlrichs, R. Adiabatic Time-Dependent Density Functional Methods for Excited State Properties. *J. Chem. Phys.* **2002**, *117*, 7433−7447.
(54) Tretiak, S.; Chernyak, V. Resonant Nonlinear Polarizabilities in the Time-Dependent Density Functional Theory. *J. Chem. Phys.* **2003**, *119*, 8809−8823.
(55) Tommasini, M.; Chernyak, V.; Mukamel, S. Electronic Density-Matrix Algorithm for Nonadiabatic Couplings in Molecular Dynamics Simulations. *Int. J. Quantum Chem.* **2001**, *85*, 225−238.
(56) Chernyak, V.; Mukamel, S. Density-Matrix Representation of Nonadiabatic Couplings in Time-Dependent Density Functional (TDDFT) Theories. *J. Chem. Phys.* **2000**, *112*, 3572−3579.
(57) Send, R.; Furche, F. First-Order Nonadiabatic Couplings from Time-Dependent Hybrid Density Functional Response Theory: Consistent Formalism, Implementation, and Performance. *J. Chem. Phys.* **2010**, *132*, No. 044107.
(58) Dewar, M. J. S.; Zoebisch, E. G.; Healy, E. F.; Stewart, J. J. P. Development and Use of Quantum Mechanical Molecular Models.

https://dx.doi.org/10.1021/acs.jpclett.0c01351
J. Phys. Chem. Lett. 2020, 11, 4711−4719

76. AM1: A New General Purpose Quantum Mechanical Molecular Model. *J. Am. Chem. Soc.* **1985**, *107*, 3902−3909.
(59) Mukamel, S. Electronic Coherence and Collective Optical Excitations of Conjugated Molecules. *Science (Washington, DC, U. S.)* **1997**, *277*, 781−787.
(60) Tretiak, S.; Chernyak, V.; Mukamel, S. Recursive Density-matrix-spectral-moment Algorithm for Molecular Nonlinear Polarizabilities. *J. Chem. Phys.* **1996**, *105*, 8914−8928.
(61) Tretiak, S.; Zhang, W. M.; Chernyak, V.; Mukamel, S. Excitonic Couplings and Electronic Coherence in Bridged Naphthalene Dimers. *Proc. Natl. Acad. Sci. U. S. A.* **1999**, *96*, 13003−13008.
(62) Tretiak, S.; Chernyak, V.; Mukamel, S. Two-Dimensional Real-Space Analysis of Optical Excitations in Acceptor-Substituted Carotenoids. *J. Am. Chem. Soc.* **1997**, *119*, 11408−11419.
(63) Tretiak, S.; Chernyak, V.; Mukamel, S. Collective Electronic Oscillators for Nonlinear Optical Response of Conjugated Molecules. *Chem. Phys. Lett.* **1996**, *259*, 55−61.
(64) Wu, C.; Malinin, S. V.; Tretiak, S.; Chernyak, V. Y. Multiscale Modeling of Electronic Excitations in Branched Conjugated Molecules Using an Exciton Scattering Approach. *Phys. Rev. Lett.* **2008**, *100*, No. 057405.
(65) Bell, R. J.; Dean, P.; Hibbins-Butler, D. C. Localization of Normal Modes in Vitreous Silica, Germania and Beryllium Fluoride. *J. Phys. C: Solid State Phys.* **1970**, *3*, 2111−2118.
(66) Taraskin, S. N.; Elliott, S. R. Anharmonicity and Localization of Atomic Vibrations in Vitreous Silica. *Phys. Rev. B: Condens. Matter Mater. Phys.* **1999**, *59*, 8572−8585.
(67) Alfonso Hernandez, L.; Nelson, T.; Gelin, M. F.; Lupton, J. M.; Tretiak, S.; Fernandez-Alberti, S. Interference of Interchromophoric Energy-Transfer Pathways in π-Conjugated Macrocycles. *J. Phys. Chem. Lett.* **2016**, *7*, 4936−4944.
(68) Soler, M. A.; Bastida, A.; Farag, M. H.; Zúñiga, J.; Requena, A. A Method for Analyzing the Vibrational Energy Flow in Biomolecules in Solution. *J. Chem. Phys.* **2011**, *135*, 204106.
(69) Paterlini, M. G.; Ferguson, D. M. Constant Temperature Simulations Using the Langevin Equation with Velocity Verlet Integration. *Chem. Phys.* **1998**, *236*, 243−252.
(70) Attard, P. Statistical Mechanical Theory for Non-Equilibrium Systems. IX. Stochastic Molecular Dynamics. *J. Chem. Phys.* **2009**, *130*, 194113.
(71) Nelson, T.; Fernandez-Alberti, S.; Roitberg, A. E.; Tretiak, S. Nonadiabatic Excited-State Molecular Dynamics: Treatment of Electronic Decoherence. *J. Chem. Phys.* **2013**, *138*, 224111.
(72) Fernandez-Alberti, S.; Roitberg, A. E.; Kleiman, V. D.; Nelson, T.; Tretiak, S. Shishiodoshi Unidirectional Energy Transfer Mechanism in Phenylene Ethynylene Dendrimers. *J. Chem. Phys.* **2012**, *137*, 22A526.
(73) Nelson, T.; Fernandez-Alberti, S.; Roitberg, A. E.; Tretiak, S. Artifacts Due to Trivial Unavoided Crossings in the Modeling of Photoinduced Energy Transfer Dynamics in Extended Conjugated Molecules. *Chem. Phys. Lett.* **2013**, *590*, 208−213.
(74) Nelson, T.; Fernandez-Alberti, S.; Chernyak, V.; Roitberg, A. E.; Tretiak, S. Nonadiabatic Excited-State Molecular Dynamics: Numerical Tests of Convergence and Parameters. *J. Chem. Phys.* **2012**, *136*, No. 054108.

https://dx.doi.org/10.1021/acs.jpclett.0c01351
J. Phys. Chem. Lett. 2020, 11, 4711−4719